Chapter 1

Satellite Combined Radar-Radiometer algorithms

Mircea Grecu[1] and
William S. Olson[2]

This chapter describes the basic components used in algorithms to derive precipitation estimates from satellite combined radar and radiometer observations. Specifically, the basic mathematical relationships connecting precipitation particle size distributions to radar and radiometer observations are succinctly, but comprehensively, described. In addition, codes to calculate radar and radiometer observations from normalized gamma size distributions and using lookup tables of electromagnetic properties at the GPM radar and radiometer's frequency are provided in a code repository located at https://tinyurl.com/COMBALG. These codes along with the elements of the optimal estimation theory presented in the chapter may be used by the reader to assemble simplified but effective radar radiometer precipitation estimation algorithms. Examples of retrievals and considerations regarding the development of combined algorithm for future satellite missions are also presented in the chapter.

1.1 Introduction

The benefit of incorporating radiometer observations into methodologies that estimate precipitation from space-borne radar observations was first realized by [1]. Specifically, due to size and weight limitations on antennae, space-borne radars operate at frequencies that make observations subject to attenuation. While attenuation correction methodologies exist, e.g. [2], variability in the distribution of precipitation particle sizes within the radar observing volume makes the attenuation correction process highly uncertain. At the same time, it had been recognized [3] that independent information regarding the Path-Integrated-Attenuation (PIA) may be used to reduce uncertainties in the attenuation correction process. PIA information independent of the radar measurements used in the attenuation correction process may be derived from the analysis of the electromagnetic power backscattered by the Earth's surface [3] and, as noted by Weinman et al. [1], low-frequency radiometer

[1]GESTAR-II, Morgan State University and NASA GSFC
[2]GESTAR-II,UMBC and NASA GSFC

observations when available. The objective of the surface analysis is to estimate the power backscattered by Earth's surface in the absence of the rain. In the presence of rain, the ratio between the actual backscattered power and the estimated clear-sky backscattered power provides an estimate of the total attenuation from the radar to the Earth's surface [3] that can be used in attenuation correction and precipitation estimation process. The problem with the PIA estimation using this approach, usually referred to as the Surface Reference Technique (SRT), is that the estimation of the no-precipitation backscattered power may be highly uncertain in some situations. As recognized by Weinman et al. [1] and even earlier investigators, e.g. [4], radiometer observations over water surfaces at frequencies not associated with significant scattering (e.g. 10- and 19-GHz) contain information strongly related to the PIA. This is because the emissivity of water surface is low and rain drops in the radiometer observing volume result in warmer brightness temperatures. The departure from the brightness temperature value expected in clear skies may be used to estimate the equivalent PIA at the radar operating frequency [1]. The initial study of Weinman et al. [1] provided a relationship between coincident radiometer observations at X-band and the associated PIA at X-band (9.6-GHz). Subsequent work by Smith et al. [5] was carried out to determine a relationship between the PIA at Ku-band (13.8 GHz) and coincident radiometer observations 10.7-GHz. This relationship was developed for use in the Tropical Rainfall Measuring Mission (TRMM) [6] combined radar-radiometer algorithm [7].

However, although the relationships between low frequency brightness temperatures and the radar PIA at X- and Ku-band are well-defined and unambiguous, the use of satellite radiometer observations in satellite radar profiling algorithms is challenging. This because the typical footprints of low-frequency radiometer observations are significantly larger than the typical footprints of space-borne radars, which makes the radiometer observations difficult to translate into radar PIA. To overcome this difficulty various approaches akin to the downscaling of the radiometer observations to the radar footprint resolution have been developed [7, 8, 9, 10]. A common feature of these approaches was that the radar-footprint PIA was not directly estimated from the radiometer observations. Instead, optimization procedures were used to minimize the differences between radiometer observations predicted from the radar observations and the radiometer observations. While the impact of the radiometer observations on the accuracy of final radar estimates is difficult to quantify, a clear benefit of combined radar-radiometer precipitation retrievals is that they are consistent with both the radar and radiometer observations. This is because the range of possible estimates that may be derived from radar-only observations is narrow down to estimates that are in agreement with the radiometer observations. Consequently, they may be used to derive large databases of precipitation and associated radiometer observations necessary in the development of "Bayesian" precipitation estimation algorithms from satellite radiometer-only observations [11, 12, 13].

1.2 Fundamental Models and Methods

1.2.1 Precipitation particles and their electromagnetic properties

To numerically characterize integral properties of precipitation (such as the precipitation rate) within a radar observing volume, a good understanding of the distributions of properties such as the size and mass of precipitation particles is necessary. Paramount to this is the concept of Particle Size Distribution (PSD). Mathematically, the PSD is a function $N(D)$ that describes the density of precipitation particles of a given size within an elementary atmospheric volume. More precisely, $N(D)dD$ is defined as the concentration of precipitation particles with sizes between D and $D + dD$ in a specified volume of air. Given expressions that relate the size of a precipitation particle to its mass and electromagnetic backscattering properties, the PSD function may be used to derive relationships between the Liquid Water Content (LWC) and radar reflectivity. In a seminal study, Marshall and Palmer [14] showed that rain Drop Size Distributions (DSDs) follow an exponential distribution, i.e. $N(D) = N_0 \exp(-\lambda D)$. Although subsequent studies showed that DSDs are generally better described by gamma functions, $N(D) = N_0 D^\mu \exp(-\lambda D)$, (see Ulbrich [15] for a review), the exponential DSD formulation of [14] represented a milestone in meteorology because it set the stage for analytical investigations of the relationships between precipitation properties and radar observations. While initially focused preponderantly on rain, as measurement techniques improved, PSD studies started addressing ice particles in the early seventies (e.g. [16, 17]). It was found that, similarly to raindrops, ice PSDs may be accurately described by gamma functions.

Equally important to the description of PSDs is the quantification of the amount of radar power backscattered by precipitation particles. To simplify the analysis, the radar measurements of returned power are converted into a related variable called the equivalent radar reflectivity factor, defined as [18]:

$$Z = \frac{\lambda^4}{\pi^5 |K_w|^2} \int_0^\infty N(D) \sigma_b(D) dD \tag{1.1}$$

where λ is radar frequency, $|K_w|$ is the dielectric factor of water, and $\sigma_b(D)$ is the backscattering cross-section of a precipitation particle of diameter D. The backscattering cross-section is the equivalent area that would isotropically return an amount of power equal to that actually returned by the precipitation particle [21]. The equivalent reflectivity factor is defined to equal $\int_0^\infty N(D)D^6 dD$ (in $mm^6 m^{-3}$) for spherical rain drops in the Rayleigh regime. That is, for spherical raindrop whose diameter D satisfy the inequality $\frac{\pi D}{\lambda} \ll 1$, the backscattering cross-section $\sigma_b(D)$ is proportional to D^6. For DSD characterized by raindrops in the Rayleigh regime, the radar reflectivity Z defined $\int_0^\infty N(D)D^6 dD$ is a very simple but meaningful variable that can be calculated analytically as a function of the DSD parameters and readily determined from the power measured by radar. Consequently, the radar reflectivity has been established as the most meaningful and convenient variable to interpret the radar return power. When the precipitation particles do not fall in the Rayleigh regime, the general formulation given in Eq. (1.1) is used to interpret observations. It should be noted that the conversion from power to reflectivity (or equivalent reflectivity) is

computationally the same, irrespective of whether precipitation particles are in the Rayleigh regime or not. However, the interpretation of observed radar reflectivity needs to account for the possibility of the precipitation particles not being in the Rayleigh regime.

When raindrops are too large relative to the radar wavelength, the Mie solution of Maxwell's electromagnetic equations is generally used to calculate $\sigma_b(D)$ [19]. While the Mie solution assumes spherical scatterers, large raindrops are oblate. Although the assumption of spherical raindrops is acceptable in many situations, there are radar applications when the oblateness of raindrops needs to be considered. In such applications, the electromagnetic properties of raindrops can be calculated using a more complex numerical methodology called the T-Matrix approach [20]. The use of the Mie solution in weather applications dates back to at least 1961 [21].

The quantification of the backscattering cross-section of ice particles is significantly more challenging than that of raindrops. This is because ice-particles exhibit a large variety of complicated shapes that preclude the application of straightforward electromagnetic equation solvers such those used in the Mie and T-matrix approaches. Before the emergence of computationally more general solvers, it was customary to assume that ice particles are spherical mixtures of ice and air characterized by an equivalent dielectric constant [21]. However, this assumption does not work well for ice particles large compared to the radar wavelength [22, 23, 24]. To address the need for accurate backscattering calculations (and electromagnetic scattering properties in general), several research groups started developing databases of ice particles and associated scattering properties using the Discrete Dipole Approximation (DDA) approach [25] and made them available to the science community at large [23, 24]. The drawback of the DDA approach is its computational cost. Specifically, the complexity of ice particle shapes precludes the use of efficient spectral solvers that make use of analytical formulae that reduce the original equations to significantly simpler equations solvable in the Fourier space [26]. As a consequence, intensive numerical calculations are necessary to quantify the electromagnetic properties of ice particles. To circumvent the intensive numerical calculates, Hogan et al. [27] developed an approach based on the Rayleigh-Gans approximation that provides computational efficient yet accurate estimates of the electromagnetic properties of ice particles at microwave frequency. When available, scattering calculations based on the DDA or other numerically intensive methods are preferable, but such calculations are not available at all frequencies, especially for new sub-millimeter wavelength radiometers that have been only recently developed or are being developed for future space missions. For such frequencies and very large ice particles relative to the instrument's wavelength, the Rayleigh-Gans approximation of Hogan et al. [27] together with the Mie-based approach of [19] and absorption models (e.g. Rosenkranz [28]) provide the ingredients necessary to simulate space-borne radar and radiometer observations from atmospheric geophysical variables.

Although valuable insight can be derived from analytical formulations of the PSDs, the increased availability of PSD observations from field campaigns eventually resulted in a paradigm shift regarding the use of the PSD observations in precipitation estimation methodologies. Specifically, it was found that a concentration

scaling parameter N_w can be derived from observations without any assumption regarding the PSD shape and used along with a geometric scaling parameter, i.e. the volume weighted D_m, to accurately characterize all relevant PSDs and the associated radar and radiometer properties [29]. The concentration scaling parameter, also known as the generalized PSD intercept [30], is defined as

$$N_w = \frac{4^4}{\pi \rho_w} \frac{PWC}{D_m^4} \tag{1.2}$$

where PWC is the equivalent precipitation (either ice or rain) water content and D_m is the volume (or mass) weighted diameter. The PSD intercept enables the expression of $N(D)$ in a compact form of the type, i.e. $N(D) = N_w h(D/D_m)$, where $h(D/D_m)$ is a rather invariant function. While $h(D/D_m)$ cannot accurately characterize all relevant PSDs. However, this normalization can account for 85% of first seven moments of the PSD [32]. One of the most consequential implications is that it can explain and mitigate variability in the relationships between radar observations and associated precipitation variables such as equivalent water content and rate. That is, representations of the joint distributions of reflectivities simulated from observed PSDs and the associated precipitation water content exhibit significant variability that makes the estimates the precipitation water content from single frequency reflectivity observations highly uncertain. Shown in the left-hand panel of Fig. 1.1 is the joint distribution of IWC and associated reflectivity at Ku-band calculated using PSD observations from the NASA IMPACTS field experiment [33]. As apparent in the panel, the joint distribution is broad with a broad range of IWC values associated with any given reflectivity. However, normalization of both IWC and reflectivity by the associated N_w makes the resulting joint (IWC/N_w, $Z(Ku)/N_w$) distribution very narrow and close to a one-to-one function. This means that IWC/N_w can be accurately predicted from $Z(Ku)/N_w$. While normalization by itself does not eliminate uncertainties, because one needs information about N_w to derive a closed form solution for IWC, it does provide a general and physical consistent framework to investigate and mitigate uncertainties in space-borne radar and radiometer retrievals. This will be explained in detail in the next section. A remarkable fact regarding the normalization by N_w is that it collapses all radar-precipitation relationships (e.g. reflectivity vs precipitation rate, attenuation vs reflectivity, attenuation vs. precipitation rate etc.) to approximate one-to-one functions for both ice and water [31]. Or, more generally, this property applies any pair of normalized variables related by a power law.

1.2.2 Radar and radiometer models

The measured radar reflectivity at range r can be expressed as a function of the true radar reflectivity at range r, $Z(r)$, and the integrated attenuation along the path [34].

$$Z_m(r) = Z(r) \exp\left(-0.2 \ln(10) \int_0^r k(Z(s)) ds\right) \tag{1.3}$$

where $k(Z(s))$ is the specific attenuation at range s. The specific attenuation may be determined as a function of an observed or assumed analytical PSD using an equation
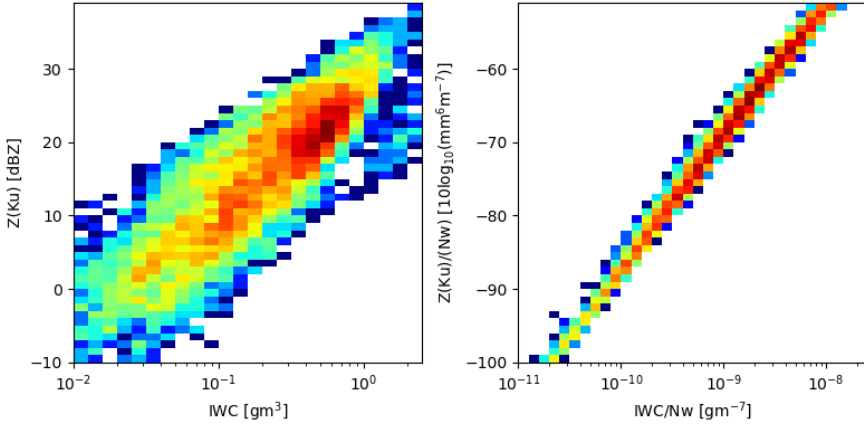
Figure 1.1   *(Left) joint distribution of ice water content (IWC) and associated Ku-band reflectivity calculated from PSD observations from IMPACTS and (Right) joint distribution of normalized IWC and Ku-band reflectivity.*

similar to Eq. (1.1), i.e. $k = \int_0^\infty N(D)\sigma_e(D)dD$, with the extinction cross-section $\sigma_e(D)$ determined using one of the electromagnetic computational methodologies described in the previous section. When the specific attenuation and the reflectivity are related through a power law, i.e. $k = \alpha Z^\beta$ with β constant with range, a closed form solution for Z exists [34], i.e.

$$Z(r) = Z_m(r)/(1 - q\int_0^r Z_m^\beta(s)ds)^{1/\beta} \tag{1.4}$$

where $q = 0.2\beta ln(10)$. This solution was first derived by Hitschfeld and Bordan [2] and started getting prominent in spaceborne radar applications with the work of [34], [35], and [36]. It should be noted that parameter β has to be constant with range for the solution to be applicable. However, β is a function of the precipitation phase and varies, although not significantly. with range. Parameter α, on the other hand, does not vary with range. This makes it possible to account for variation in β by variations in α [34].

A particular challenge in applying Eq. (1.4) to radar observations affected by significant attenuation is that the numerical value of term $q\int_0^r Z_m^\beta(s)ds$ may become larger than 1.0, in which case the equation is not applicable anymore. Moreover, even if $q\int_0^r Z_m^\beta(s)ds < 1$ the path integrated attenuation associated with Eq. (1.4) may not be in agreement with estimates from a Surface Reference Technique (SRT) analysis. This is discussed in [34] and [36]. Several ad-hoc techniques were developed to reconcile solution 1.4 with the SRT estimates, but, fundamentally, the problem was not satisfactorily addressed from the physical perspective until the work of Ferreira et al. [31]. Ferreira et al. [31] noted that all $k - Z$, $Z - R$ or $Z - PWC$ (where k is the specific attenuation and Z, R and PWC are the associated reflectivity, precipitation

rate and precipitation water content) are exact for a given constant N_w. They also noted that more general relationships, explicitly accounting for the N_w variability, need to be derived and used to make the Hitschfeld-Bordan solution in Eq. (1.4) consistent with SRT estimates of Path Integrated Attenuation (PIA). Specifically, a more general $k - Z$ relationship of the type

$$k = N_{w,rel}^{1-\beta} \alpha Z^{\beta} \tag{1.5}$$

where $N_{w,rel}$ is the ratio of actual N_w to that of the reference N_w^0 for which the relation $k = \alpha Z^{\beta}$ holds perfectly may be derived and used with 1.4. The PIA attenuation associated with the generalized $k - Z$ relation in 1.5 is

$$PIA_{HB}(N_{w,rel}) = -10/\beta \log_{10}(1 - q N_{w,rel}^{1-\beta} \int_0^{r_s} \alpha Z_m^{\beta}(s)ds) \tag{1.6}$$

Given an independent estimate of PIA from the SRT, PIA_{SRT}, one may determine the value of $N_{w,rel}$ that satisfy $PIA_{HB}(N_{w,rel}) = PIA_{SRT}$. This provides a physical approach to reconcile the Hitschfeld-Bordan solution with a potentially different SRT PIA estimate [31]. The benefit of this approach relative to more ad-hoc approaches such as the α adjustment method [34] is that it enables the adjustment of the $Z - R$ (or $Z - PWC$) used in the estimation of precipitation rates (or equivalent water contents) from the attenuation corrected reflectivities [31]. This is because systematically different mean particle sizes may result not only in biased attenuation correction, but also in biased precipitation estimates due to the application of a biased reflectivity precipitation relationship. Therefore, the benefit of using N_w-based relationships is twofold [31].

A simple implementation of the Hitschfeld-Bordan solution in the Python programming language is given listing 1.1 and available online at https://tinyurl.com/COMBALG.

```python
def hb(Zm, Nrel , alpha , beta , dr ) :
    q=0.2*np . log (10)
    eps=Nrel **(1 − beta )
    zeta=q*beta *eps*alpha *10**(0.1*Zm*beta )*dr
    zetaSum=zeta . cumsum ( ) [ −1]
    if zetaSum >0.995:
        f =0.995/ zetaSum
    else :
        f =1
    Zc=Zm−10/ beta *np . log10 (1−f *zeta . cumsum ( ) )
    pia =−10/ beta *np . log10 (1−f *zeta . cumsum ( ) )
    return zc , pia , f
```

Listing 1.1   Python implementation of the Histchfeld-Bordan solution.

where Zm and Zc are the observed and attenuation corrected reflectivity vectors, alpha and beta are α and β, Nrel is $N_{w,rel}$, and dr is the range bin size. Although this attenuation-correction implementation is deliberately simple to facilitate comprehension, it has all the ingredients required for practical application. In practice, it

is possible that $\zeta(r_s) = qN_{w,rel}^{1-\beta}\int_0^{r_s}\alpha Z_m^\beta(s)ds \geq 1$. In such situations, the Hitschfeld Bordan approach does not work for ranges beyond the range value where $\zeta(r) = 1$. This behavior, which is a consequence of the accumulations of errors in the attenuation estimation and correction process, may be mitigated by simply rescaling $\zeta(r)$ by a factor f that makes $f\zeta(r)$ smaller than 1.0 for any $r < r_s$. It is worth mentioning that the $\zeta(r)$ adjustment technique is used in all forward Hitschfeld-Bordan attenuation-correction algorithms (eg. [34],[38], [37]), although notations and computational procedures may vary from case to case. Moreover, the interpretation of the physical meaning of the f factor is also variable. A possible interpretation is that $f \neq 1.0$ is indicative of an N_w value different from that used in the derivation of the $k - Z$ relationship. To reconcile the N_w value used in the attenuation correction with the final PIA_{HB}, one can rescale it by $f^{\frac{1}{1-\beta}}$.

It should be noted that because neither the SRT estimates nor the Hitschfeld-Bordan predictions of PIA are perfect, equating them exactly is suboptimal because it attributes various types of uncertainties to variability in the N_w. A better approach is to adjust N_w such that the final PIA_{HB} is consistent with both the uncertainties in its initial values (prior to the SRT based adjustment) and the PIA_{SRT} uncertainties. Iguchi et al. [38] developed such a methodology based on Bayes estimation theory. However, Iguchi et al. [38] did not update the Hitschfeld-Bordan solution in terms of N_w, but in terms of an equivalent variable ε, and it was Ferreira et al. [31] who made the connection between SRT estimates and N_w adjustments. A similar N_w-ε connection is used in the GPM DPR algorithm [37].

The use of normalized $k - Z$ and Z-precipitation relation is beneficial even when SRT PIA estimates are not available but additional sources of information, such as coincident radiometer observations are available. Specifically, if a set of observations $\mathbf{Y_{obs}}$ independent of the radar observations used in a radar-only precipitation profiling algorithm, one may tune the N_w assumptions made in the radar-only profiling algorithm to maximize the agreement between them and their prediction from the radar-only estimates. Or, more precisely, an objective function may be defined as

$$F(\mathbf{N_w}) = \frac{1}{2}(\mathbf{Y_{obs}} - \mathbf{Y}(\mathbf{Z_m}(\mathbf{N_w})))^{\mathbf{T}}\mathbf{W_Y^{-1}}(\mathbf{Y_{obs}} - \mathbf{Y}(\mathbf{Z_m}(\mathbf{N_w})))+$$

$$\frac{1}{2}(\mathbf{N_w} - \mathbf{N_w^0})^{\mathbf{T}}\mathbf{W_N^{-1}}(\mathbf{N_w} - \mathbf{N_w^0}) \quad (1.7)$$

where $\mathbf{Y}(\mathbf{Z_m}(\mathbf{N_w}))$ is a numerical model that predicts observations $\mathbf{Y_{obs}}$ as a function of the space-borne radar observations $\mathbf{Z_m}$ and the normalized N_w intercepts. Matrix $\mathbf{W_Y^{-1}}$ quantifies uncertainties in model $\mathbf{Y}$, while $\mathbf{N_w^0}$ and $\mathbf{W_N}$ are the climatological values of $\mathbf{N_w}$ and their associated covariance matrix. Note that $\mathbf{Y_{obs}}$ may consist of any useful combination of space- or ground-based observations, while the set of $\mathbf{N_w}$ may need to be extended to include other geophysical variables relevant in the prediction of $\mathbf{Y}$. From the mathematical perspective, the problem of determining $\mathbf{N_w}$ from $\mathbf{Y_{obs}}$ is generally ill-posed and additional climatological, or "a priori" in statistical terminology, information is needed to derive a unique solution [39]. The additional information is provided by the second term of the objective function in Eq. (1.7). An implementation of a combined radar-radiometer estimation algorithm

based on Eq. (1.7) and applicable to airborne observations was developed by Grecu and Anagnostou [40]. An evaluation based on synthetic observations derived from cloud resolving model simulations indicated the superiority of combined retrievals relative to radar-only retrievals. A potentially more general approach, i.e. considering a larger set of state variables, but computationally more intensive and prone to challenges when used in operational environment had been developed by Marzano et al. [41]. Specifically, the state variables in [41] included the precipitation water contents while the radar observations were not implicitly satisfied but included in the optimization problem. A comprehensive discussion on why an approach with a reduced number of variables and the radar observations at a given frequency automatically satisfied is beneficial is provided in [40].

Irrespective of whether single-frequency radar observations are included in the objective function or automatically satisfied, it should be noted that the use of additional information enables in theory the derivation of more accurate estimates of additional variables, such as the normalized PSD intercepts, that in the worst case scenarios are simply set up based on their climatology. To estimate the state variables in Eq. (1.7), a computationally efficient model to simulation the observations **Y** and an optimization procedure are needed. The simulation of air- and space-borne radiometer requires a procedure to solve the radiative transfer equation, which in the plane-parallel approximation reads [42].

$$\mu k_{ext} \frac{dI(\mu, \phi)}{dz} = -I(\mu, \phi) + (1-a)B(T) +$$

$$\frac{a}{4\pi} \int_0^{2\pi} \int_{-1}^1 p(\mu, \phi, \mu', \phi') I(\mu', \phi') d\mu' d\phi' \quad (1.8)$$

where $I(\mu, \phi)$ is the intensity in direction given by μ (the cosine of the angle between the actual direction and the vertical axis) and azimuthal angle ϕ, k_{ext} is the extinction coefficient, a is the scattering albedo (the ratio of the scattering coeffcion to the extinction coefficients), $B(T)$ is the black body radiation emitted by the atmosphere at temperature T and the radiometer's frequency and $p(\mu, \phi, \mu', \phi')$ is the scattering function. The most general solvers of the radiative transfer equation are computationally intensive. However, the assumption of no azimuthal dependence and the approximation of I and $p(\mu, \mu')$ using the first two terms of a Legendre series [42] reduce the initial equation to a system of two coupled ordinary differential equations [42]. Systematic evaluations between the approximate solution and more general solutions revealed differences that can be mitigated through simple modifications that account for geometric effects in the approximate solution [43].

The relevant coefficients in Eq. (1.8) are determined through the integration of the absorption, scattering and phase function properties of individual particles for given observed or analytical PSDs. A file containing the integrated scattering properties used in the Global Precipitation Measurement (GPM) combined algorithm [44] is available in netCDF format at:
https://github.com/mgrecu35/IET_bookChapter/tree/main/lookupTables. The properties of four types of hydrometeors, i.e. rain, snow, graupel and hail, are included in the file. Properties are calculated assuming normalized gamma particle size dis-

tributions with μ=2 and N_w=0.08cm^{-4}. The mean mass diameter, precipitation rate, and precipitation water content associated with each entry are also included in the file. The rain, graupel and hail properties are calculated using the Mie approach, while the snow properties are derived from DDA calculations. Additional information is provided in the README.md in the lookup table directory. An implementation of plane-parallel radiative solver of the [42] is available in directory src of https://github.com/mgrecu35/IET_bookChapter/. The reader is encouraged to pull the entire directory and examine the files in subdirectory examples. These files provide examples of radar and radiometer calculations using the concepts described in the chapter. The examples require a working version of Python and some specific libraries. Instructions on how the installation of the required libraries are provided in the README file in the examples directory. An example of Python code to derive Ka-band radar and precipitation properties as a function of the true Ku-band reflectivity using information stored in the lookup tables is show in listing 1.2

```python
def getRainProp(zKuTrue,log10dnw,lookUpTable):
    if zKuc>12:
        ibin=int((zKuTrue-10*log10dnw+12)/0.25)
        if ibin<=0:
            ibin=0
            dnw=(zc+12)/10.
        if ibin>=288:
            ibin=0
            dnw=(zc-lookUpTable.zKaR[288])/10.
        zKa=lookUpTable.zKaR[ibin]+10*log10dnw
        attKa=lookUpTable.attKaR[ibin]*10**log10dnw
        pRate=lookUpTable.rainRate[ibin]*10**log10dnw
    else:
        zKa=-99
        attKa=0
        pRate=0
    return zKa,attKa,pRate
```

Listing 1.2   *Python implementation of a scattering lookup table interface function.*

where zKuTrue is the true Ku-band reflectivity, log10dnw is the log10 of the relative N_w intercept and lookUpTable is the object containing scattering and precipitation information. The Ku-band reflectivity are stored sequentially in 0.25 dB apart entries starting at -12 dBZ and ending at 60 dBZ. Each Ku-band reflectivity entry contains the associated PSD information (e.g. D_m, precipitation rate, precipitation water content, etc.), the reflectivity and attenuation at Ka-band, the extinction and scattering coefficients, and the asymmetry factor at all radiometer frequency and for all phases. This makes the navigation of the lookup table straightforward as apparent in listing 1.2.

1.2.3   Elements of optimal estimation theory

According to Gelb [45], an optimal estimator is a computational algorithm that processes measurements to deduce a minimum error (in accordance with some stated criterion of optimality). Based on this classical definition, any estimate that results from the minimization of an error-related objective function like the that in Eq. (1.7) is optimal. Nevertheless, because the minimization of observations errors is usually insufficient in deriving accurate estimates, additional terms called regularization terms [48] need to be included in the objective functions. An effective and meaningful type of regularization may be achieved through the use of Bayes' Theorem [49]. Bayesian optimal estimation is preferable to other types of regularizations when the variables to be estimated have well-defined physical meanings and their statistical properties may be systematically studied independently of the estimation problem at hand. This is the case for combined radar radiometer retrievals because the distributions of PSD intercepts can be independently studied and characterized using ground observations and/or numerical models.

Another element specific of optimal estimation procedures is their reliance on an optimization procedure. This is the reason why optimal estimation procedures are not always the method of choice in applications. Specifically, in some applications, the optimization problem associated with the estimation problem is so complicated that alternative (theoretically inferior) approaches are preferred.

The most general optimal estimation theory framework involves a state variable vector including all geophysical variables needed to simulate the radar and radiometer observations. However, that is problematic from practical perspective because the number of iterations required to derive a solution is large and make the approach computationally intensive. A more practical approach is to consider a reduced set of variables to be optimized and use the Ku-band radar observations as constraints [40]. Specifically, given that the Hitschfeld-Bordan approach [2] provides a reliable solution as a function of the vertical distribution of the normalized intercept $\mathbf{N_w}$, one can derive explicit Hitschfeld-Bordan solutions and optimize them as a function of $\mathbf{N_w}$ [40]. For combined radar-radiometer retrievals, the optimality criterion is the minimum of the objective function in (1.7) that measures the agreement between simulated and observed brightness temperatures, radar reflectivities at additional frequencies and PIA.

Even though the reduced state variable formulation is simpler, the minimization of $F(\mathbf{N_w})$ is still a computationally challenging problem. This is true especially when the radiometer footprint size is significantly larger than that of the radar footprint size. Moreover, the simulated and observed brightness temperatures at some frequencies may be in poor agreement because of other variables, such as the surface emissivity, the vertical cloud water distribution, etc., and the state variable vector $\mathbf{X} = \mathbf{N_w}$ needs to be extended to include these variables. Although still simpler than a problem that, in addition to $\mathbf{N_w}$, includes $\mathbf{D_m}$ as an independent variable and the observed Ku-band reflectivity as observations rather than constraints, the optimization associated with the combined retrieval is still rather a computationally difficult problem. This is because the most efficient optimization problem solvers require the gradient calculations (i.e. the derivative of the objective function with respect to the

state variable) [46]. The naive evaluation of the gradient is computational expensive, but special techniques involving reverse evaluations may be used [40]. The challenge with reverse evaluation is that they are not as intuitive as the forward implementation of the physical models involved in the retrievals and are prone to implementation errors if manually coded. Software programs to automatically derive the reverse gradients from the forward objective function implementation [40] exist, but they may run into efficiency issues for objective functions involving complex forward models. An alternative to the analytical linearization of the objective function is the statistical linearization [45]. A particular statistical linearization approach that has become extremely popular in the last 20 years is the Ensemble Kalman Filter [47]. In a nutshell, the approach consists of statistically perturbing the state variables and calculating an ensemble of observations associated with the perturbed state variables. Instead of explicitly evaluating the gradient of the objective function and using a gradient-based method to minimize it, a second order minimization formulation that derives the solution based on second order (quadratic) approximation is used. The solution is formally identical to the extended Kalman filter [47]. However, the derivative of the physical models with respect to the state variables are not explicitly evaluated. Instead, the Kalman gain [47] is directly derived and used in the solution. The specific steps may be summarized as follows:

- Generate an ensemble of PSD intercepts $\mathbf{N_w}$ and other geophysical variables included in the state variable vector.
- Derive radar-only precipitation estimation from the Ku-band radar observations.
- Simulate radiometer, additional frequency radar (if multiple radar observations are available) and SRT PIA observations.
- Apply an Ensemble Kalman Smoother

$$\mathbf{X} = \mathbf{X} + \mathbf{cov}\langle \mathbf{X}, \mathbf{Y} \rangle (\mathbf{cov}\langle \mathbf{Y}, \mathbf{Y} \rangle + \mathbf{R})^{-1}(\mathbf{Y_{obs}} - \mathbf{Y}(\mathbf{X})) \qquad (1.9)$$

to update the solution, where $\mathbf{X}$ is the state variable vector, $\mathbf{Y}$ is the simulated observations vector, and $\mathbf{cov}\langle \mathbf{X}, \mathbf{Y} \rangle$ is the covariance of $\mathbf{X}$ with $\mathbf{Y}$. $\mathbf{cov}\langle \mathbf{Y}, \mathbf{Y} \rangle$ is the covariance of $\mathbf{Y}$ with itself, $\mathbf{Y_{obs}}$ is the observation vector, and $\mathbf{R}$ is the observational and modeling uncertainty.

The ensemble approach is used in the GPM combined algorithm [44].

1.2.4 Additional matters
1.2.4.1 Non-uniform beam filling and multiple scattering

It goes without saying that the optimal estimation theory is not likely to result in unbiased estimates if the models involved in the estimation are biased. Specifically, models to calculate space-borne radar observations at Ka-band need to account for potential non-uniform beam filling (NUBF) and multiple scattering effects to mitigate biases in the estimates. This is because non-homogeneity in the distribution of precipitation in the radar observing volumes do not cancel out in the observation space due to the fact that the energy backscattered by precipitation particles in a certain volume is not linearly related to the amount of precipitation in that volume. Moreover, energy backscattered by precipitation in atmospheric volumes relatively

close to one another may be subject to significantly different degrees of attenuation [50], which makes NUBF effects increase with frequency. To mitigate NUBF effects, Monte Carlo methodologies based on the downscaling of observations and retrievals at finer scale may be used. Such a methodology has been developed for and implemented in the GPM combined algorithm [44]. Specifically, given a profile of Ku-band radar reflectivity observations, a set of profiles is statistically generated such that their average in the natural space yields back the original profile. Hitschfeld Bordan precipitation estimates are derived for every statistically generated Ku-band observation profile and the associated Ka-band radar observations are calculated and aggregated back to the original radar resolution. It was found that, depending on the degree of assumed variability with the radar footprint the resulting Ka-band reflectivity profiles may be significantly different from the one calculated assuming no variability within the radar observing volumes [44]. Similar behaviour was found for the calculated Ka-band PIA. The parameters of the downscaling model developed in [44] were determined by trial and error, but found to be biased and updated in subsequent versions of the GPM combined algorithm. Moreover, it was found that multiple scattering effects, that consist of multiple interactions of radar emitted energy with precipitation particles before reaching the radar receiver, may be significant at Ka-band. A computationally efficient model to account for multiple scattering effects in radar observations was developed by Hogan and Battaglia [51] and implemented in the GPM combined algorithm [44]. The model can readily calculate radar observations accounting for higher interactions between the energy emitted by the radar and precipitation particles as a function of precipitation electromagnetic scattering properties such as the extinction and scattering coefficients, the asymmetry factor and the unattenuated reflectivity. These properties may be obtained from the scattering lookup tables using procedures similar to that outlined in listing 1.2.

An example of Ku-band radar observed reflectivity profile from the Global Precipitation Mission (GPM) [53] is shown in 1.2.4.1. The Ka-band reflectivity profiles derived from the Ku-band estimates using three different models are also shown in the figure. The first model, indicated as $Z_{sim}(Ka)$ in the figure, is a simple single-scattering model that does not account for either NUBF or multiple scattering effects. The second model, $Z_{NUBFsim}(Ka)$, accounts for NUBF effects, while the third, $Z_{MS}(Ka)$ accounts for multiple scattering effects using the of [51]. Note that the difference between the model that accounts for multiple scattering and those that do not are extremely large. In the absence of such a model, the optimal estimation framework would interpret the differences between simulated and observed Ka-band reflectivities as severe attenuation at Ka-band and would adjust the solution to one characterized by significantly less attenuation. The adjusted solution would be associated with significantly smaller precipitation rates (or equivalent water contents). In reality, while the attenuation is indeed severe at Ka-band, the associated reflectivities are significantly enhanced by multiple scattering effects. The impact of NUBF on simulated reflectivities is not as significant as that of multiple scattering for this particular example, but it may be for shallower but more intense precipitation. Moreover, the NUBF model has an impact on the interpretation of the PIA estimated using
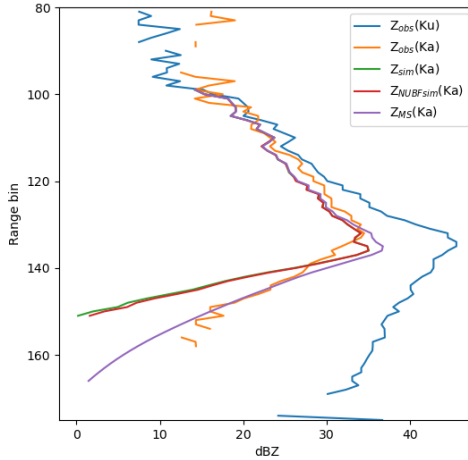
Figure 1.2   Example of Ka-band reflectivity profile calculated from Ku-band-only precipitation estimates. Multiple Ka-band reflectivity models are included, i.e. single scattering model, single model accounting for NUBF, and multiple scattering model.

the SRT. Specifically, the apparent SRT PIA may be 20% to 50% smaller than the value associated with uniform extinction within the radar observing volumes.

1.2.4.2   Radiance preprocessing

As previously mentioned, a particular challenge in the derivation of precipitation estimates from combined radar and radiometer observations stems in the fact that the radiometer footprint size is significantly larger than that of the radar. To mitigate this challenge, one may treat the problem as a large scale optimization problem and simultaneously process the observations from multiple radar scans and the associated brightness temperatures. In this case, the brightness temperatures simulated from the radar retrievals are convolved to the radiometer footprint resolution and the radar retrievals are updated to improve the consistency between simulated and observed brightness temperatures at radiometer footprint scale. While mathematically this is the best approach, it is computationally challenging, without guaranteeing significantly better results than simpler approach due to uncertainties in the forward model and limited informational content in the observations. A simpler solution, although theoretically more prone to uncertainties, is to deconvolve the radiometer observed brightness temperatures to the radar footprint resolution and derive estimates by sequentially processing radar observations profiles. This approach is used in the GPM combined algorithm [44]. Specifically, [44] use simulations to derive a multivariate regression to estimate the radiometer brightness temperature at radar footprint size resolution from the actual radiometer observations within a window centered on

the radar footprint's position. Although the approach works satisfactorily within the GPM combine algorithm is expected that more advanced methodologies based on deep learning [52] would be more effective in deconvolving the observed radiometer observations.

1.3   GPM combined observations and retrievals

1.3.1   Observations

Shown in figure 1.3.1 is an example of observations from the GPM mission. Specifically, observed reflectivity from the Dual Frequency Precipitation Radar (DPR) and two of the associated brightness temperatures from the GPM Microwave Imager (GMI) [53] for a portion of orbit 5866 over the Kwajelein atoll are shown. As apparent in the figure, at reflectivity observations tend to be significantly attenuated at Ka-band. Some scans exhibit attenuation even at Ku-band. As discussed in the previous sections, the reflectivity observations need to be corrected for attenuation to be usable in the derivation of precipitation estimates. Independent estimates of the PIA from the application of SRT method are extremely important in the attenuation-correction process. However, reliable SRT PIA estimates are not always available, especially when only single frequency radar-observations are available and the attenuation is low relative to the noise in the estimates. An assessment of the accuracy of the DPR PIA estimates from the single and dual frequency SRT method is provided in [55]. The 18.7-GHz brightness temperatures for orbit 5866 over the Kwajelein atoll are also shown in the bottom panel of Fig. 1.3.1. As explained in the previous section brightness temperatures at X-band and higher frequencies may be used to estimate provide alternative PIA estimates. Such estimates are especially useful when the SRT PIA estimates are unreliable. However, they may be used in the estimation process along with SRT PIAs, because the optimal estimation theory can effectively incorporate information from multiple sources as long as their uncertainties are properly specified. The 18.7-GHz brightness temperatures are in qualitative agreement with the radar observations, i.e. they tend to increase in regions where the radar observations suggest high intensity precipitation and significant attenuation and attain their minimum values in regions where the radar does not detect any precipitation. However, the 18.7-GHz exhibit significantly smoother along track variability than the radar observations. This is because the GMI's footprint size at 18.7-GHz is significantly coarser than the DPR's footprint size. Specifically, the GMI's footprint resolution at 18.7-GHz is 11.0 km in the along-scan direction and 18.0 km in the cross-scan direction [54], while that of the DPR is 5.0 km. As described in the previous section, various approaches such as deconvolution or the convolution of DPR footprint simulated brightness temperatures and the evaluation of brightness temperatures errors at the radiometer's footprint resolution may be used to account for the radar and radiometer's footprint size discrepancies.
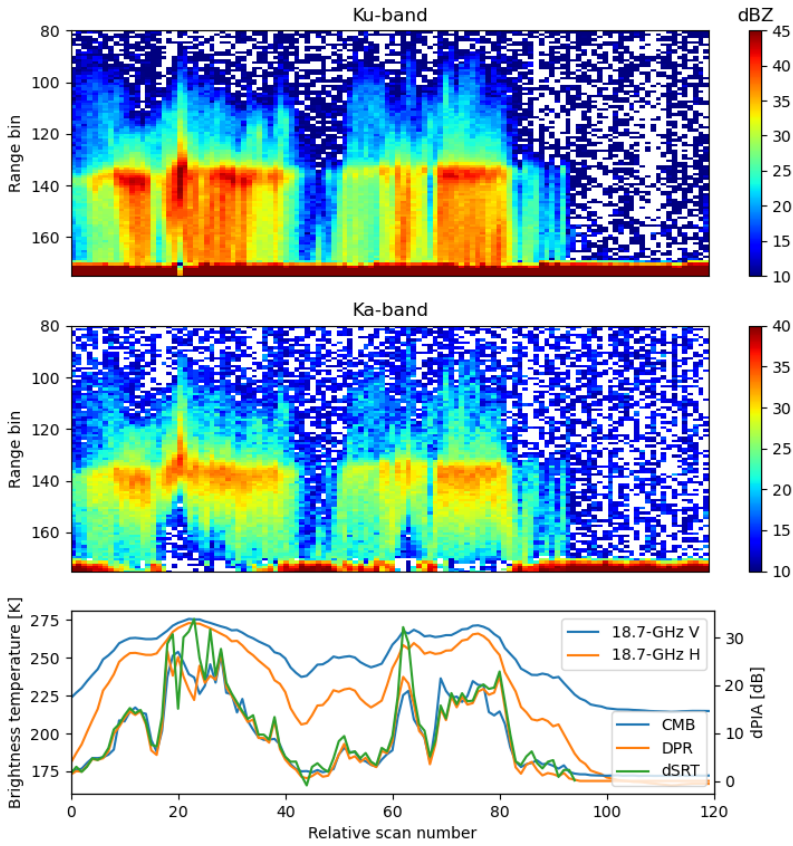
Figure 1.3   Example of observed DPR Ku-(top), Ka-band reflectivities (middle), and GMI 18.7-GHz brightness temperatures (bottom).

1.3.2   Machine learning based evaluation

Insight into the utility of brightness temperature information in the estimation of the PIA may be derived using a Machine Learning (ML) [57] approach. Specifically, a nonlinear regression may be derived to statistically estimate the PIA at the DPR frequencies from GMI brightness temperatures. This idea was already explored by [5] for the TRMM instruments, but instead of simulated brightness temperatures and PIA, one can use actual GMI observations and accurate PIA estimates from the dual SRT [55]. While PIA estimates derived from observed brightness temperature cannot be more accurate than dual SRT PIA estimates used in the development of the statistical relationships upon which they are based, they are extremely useful when accurate dual SRT PIA estimates are not available. That is prior, to 21 May 2018, GPM dual frequency radar observations were collected only across half of entire single frequency swath [58]. This is because the GPM Ka-band frequency radar collects observations in two modes, and both modes were focused on the near nadir portion of the scan prior to 21 May 2018 when a scan pattern change was implemented to enable the collection of dual-frequency observations across the entire DPR swath. This means that dual SRT PIA estimates were not available across the entire DPR swath before the scan pattern change. Therefore, a statistical relationship to estimate the dual SRT PIA from orbserved brightness temperatures does not have only theoretical but also practical value. Moreover, the Tropical Rainfall Measuring Mission (TRMM) PR was a single frequency radar [6] and the fraction of reliable SRT PIA estimates from single frequency observations is significantly smaller than that from dual frequency observations. Thus, a statistical brightness temperature PIA relation is extremely beneficial to TRMM precipitation estimates. At the same time, it is expected that future space borne radars will have Doppler capabilities but not dual Ku-Ka frequency capabilities. In short, there are multiple benefits in deriving and investigating a relationship between the observed GMI brightness temperatures and dual SRT PIA estimates, although such a relationship is not currently used in the GPM combined radar radiometer algorithm [44].

Mathematically, the derivation of a parametric regression between two set of variables $\{\mathbf{X_1}, \mathbf{X_2}, ..., \mathbf{X_n}\}$ and is $\{\mathbf{y_1}, \mathbf{y_2}, ..., \mathbf{y_n}\}$ is equivalent to the determination of a function f of variables X and parameters Θ that maximizes the agreement between $f(\mathbf{X_i}, \Theta)$ and y_i. The agreement between $f(\mathbf{X_i}, \Theta)$ and y_i is evaluated through typical mathematical functions called loss functions [59]. Function f consists of a sequential composition of rather elementary functions [59]. Multiple software libraries that allow the definition of function f and the determination of parameters Θ with minimum effort exist. In this chapter, the TensorFlow machine learning library [60] is used to derive a model to estimate the differential PIA from observed GMI observations. The model is based on a simple feed forward architecture with four hidden layers consisting of eight neurons [59]. Alternatives architectures were considered, but, given the simplicity of data, no significant variations in performance was found as long as the network had sufficient neurons (on the order of hundreds) to encode the information in the training dataset. The training dataset consists of about 180,000 records of observed GMI brightness temperatures over oceans and associated differential SRT PIA estimates, while the evaluation dataset consists of about
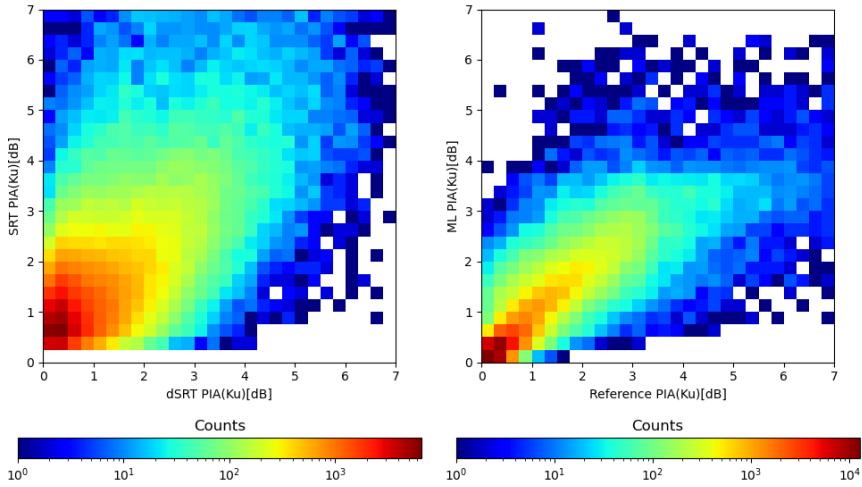
Figure 1.4   (Left) Ku-band PIA estimates from the single frequency SRT analysis against Ku-band PIA estimates from the single frequency SRT analysis. Brightness- temperature ML-based PIA estimates against reference PIA estimates from both single and dual-frequency SRT analysis.

90,000 records. Shown in the right panel of Fig. 1.3.2 is the joint distribution of the PIA(Ku) estimated from observed radiometer observations and the PIA(Ku) estimated using the differential SRT. As apparent in the figure, the agreement between the ML and the differential SRT estimates is good. The frequency of ML PIA(Ku) estimates that exceeded 4 dB appears to be notable lower than that of differential SRT estimates exceeding 4 dB, which is most likely of consequence of the coarse resolution of the low frequency radiometer observations. That is, given its coarse resolution, there is a significant variability of precipitation within a radiometer foot-print. The exact location of precipitation maxima is difficult to pinpoint especially using point estimators that do not incorporate spatial information. Nevertheless, the ML estimator's deficiency in estimating PIAs larger than 4 dB is not a significant drawback in practice because single frequency SRT PIA estimates tend to be reliable when PIA is larger than 4 dB [56]. At the same time, single frequency SRT PIA estimates tend to be unreliable for small PIA values. Thus, the ML and single frequency SRT PIA estimates work best in tandem, by complementing each other. For context, the joint distribution of single and differential SRT PIA estimates are shown in the left-hand panel of 1.3.2. As apparent in the figure, the agreement between ML and differential SRT PIA estimates is better than that between single and differential SRT estimates. This is not surprising, given that the random component of the single frequency SRT PIA error is rather large [56].

1.3.3 Combined estimates

Shown in the top panel of Fig. 1.3.2 is differential PIA estimated by the ML model described in the previous section using the radiometer observations associated with the GPM case show in Fig. 1.3.1. Over-plotted are the estimates from the differential and single frequency SRT methods. The official DPR Version 7 differential PIA estimates (labeled as DPR in the figure) along with a range of estimates (labeled HB) derived using the Histchfeld Bordan approach implemented in listing 1.1 and supporting routines in the chapter code repository are also shown in Fig. 1.3.2. As apparent in the figure, the various estimates are generally in good agreement, with the exception of two regions around relative scan numbers 20 and 60. These regions are characterized by large attenuation, which is apparent in the Ka-band observations shown in Fig. 1.3.1. As previously mentioned, when the attenuation is very large, neither differential SRT-based nor brightness temperature based PIA estimates are reliable due to the saturation effects. That is observations involved in the estimation process do not exhibit any more changes in magnitude when the integrated attenuation exceeds a certain threshold. In such situations, the single frequency SRT PIA estimates are most reliable. While an optimal estimation framework such that the ensemble methodology outlined in the previous section can incorporate multiple estimates of the same variable, the specification of the uncertainties associated with those estimates is challenging in practice because errors tend to have distributions significantly more complex than a normal distribution. However, irrespective of how uncertainties are specified and which estimate is deemed the most reliable, PIA information is essential in narrowing down the distribution of possible Hitschfeld-Bordan precipitation and associated PIA estimates.

Shown in the bottom panel of Fig. 1.3.2 are the surface precipitation estimates associated with the Hitschfeld-Bordan solutions shown in the top panel of the figure and a surface precipitation estimate derived by adjusting the PSD N_w to a value that maximizes the agreement between the associated PIA and the estimates from the ML model and the Ku-band SRT method. The Ku-band SRT PIA estimates are incorporated only in the estimation of convective precipitation. In this illustrative example, N_w is assumed vertically constant in the rain phase, and increasing with height in the ice phase using a relation derived from PSD observations from the IMPACTS field campaign [33]. The Hitschfeld-Bordan PIAs are calculated as a function of N_w, i.e. $PIA_{HB}(N_w)$, and N_w is updated based on the ML PIA estimate (and the Ku-band SRT PIA estimates for convective rain) using the methodology described in the previous section. As apparent in the figure, the initial range of possible surface precipitation estimates is broad. The climatology of N_w varies significantly around the globe and as a function of season, and just setting N_w based on its climatology results in large uncertainties. This is why independent information on PIA is crucial in mitigating biases and uncertainties in space borne radar retrievals. As demonstrated in this and the previous subsection, brightness temperature observations may be used to derive reliable PIA estimates and significantly impact the space borne radar precipitation estimates when reliable SRT PIA (or differential SRT PIA) estimates do not exist. Differential SRT PIA estimates are generally reliable over oceans, but not all space borne Ku-band radar observations are associated with collocated Ka-band radar ob-
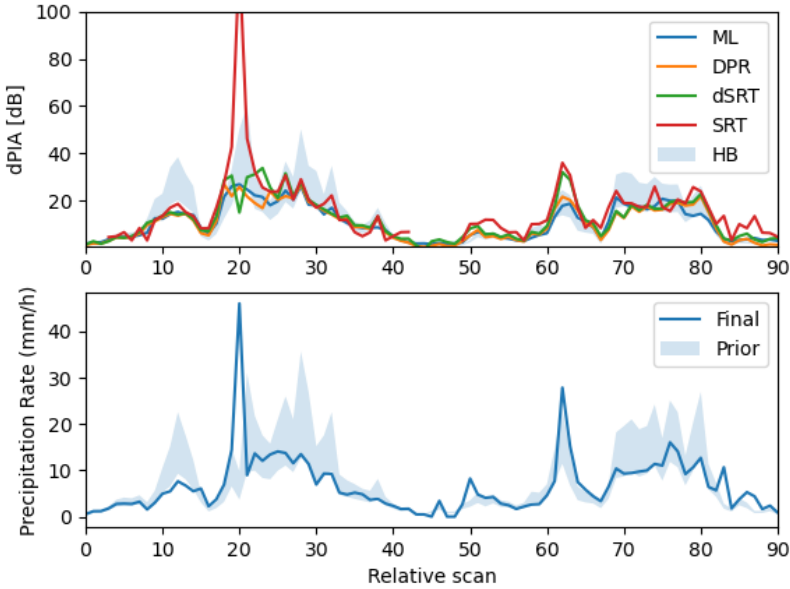
Figure 1.5 *(Top) Differential PIA estimates from the ML model, the official DPR version 7 algorithm, the dual and single frequency (Ku) SRT method associated with the observations in Fig. 1.3.1. A range of Hitschfeld-Bordan PIA derived using N_w two times larger and smaller than the reference value of $0.08cm^4$ is also shown.(Bottom). The surface precipitation estimates from the Histchfeld-Bordan approach associated with the PIAs shown in the top panel (labeled Prior) and the optimal surface precipitation estimate (labeled Final).*

servations to enable the derivation of differential SRT estimates. This is the case for TRMM radar observations and GPM radar observations outside the matched scan before the scan pattern change. The brightness temperature observations are expected to be extremely consequential for such radar observations.

1.4   Summary and conclusions

In this chapter, the basic theoretical and practical concepts associated with the development of algorithms to derive precipitation estimates from satellite combined radar and radiometer observations are discussed. Concepts include particle size distributions and their relations to radar and radiometer observations, and elements of the optimal estimation theory. Computer codes to numerically explore the concepts described in the chapter are provided in a code repository located at

https://tinyurl.com/COMBALG. These codes may be used by the reader to derive relatively simple but insightful radar radiometer precipitation estimation algorithms.

The initial motivation behind the development of combined radar-radiometer algorithms stemmed in fact information about the path-integrated attenuation associated with observations from space-borne radars operating at attenuating frequency may be obtained from collocated brightness temperatures. This fact and its implication on the estimation of surface precipitation rate is illustrated in the chapter. Additional motivation stems in the need to build databases of precipitation variables and physically consistent associated brightness temperatures to support the development of radiometer precipitation algorithms.

It is envisioned that satellite combined radar and radiometer retrievals will be of paramount importance for the development of precipitation estimation algorithms for future mission sensors. This is because future missions are likely to include a variety of new sensors that are significantly smaller, less expensive and easier to deploy than existing ones [61, 62, 63]. However, miniaturization and affordability tends to be associated with higher-frequencies and more indirect observations. As a consequence, more advanced algorithms are necessary to derive precipitation estimates are accurate as those derived from more traditional satellite instruments. These algorithms are likely to require supporting 3D precipitation databases that can be used for either regularization in the case of traditional optimal estimation framework or for the calculation of synthetic satellite observations and the development ML inversion techniques. Such databases may be derived from existing products and methodologies through the inclusion and validation of forward observations models relevant to the new instruments. From this perspective, combined radar-radiometer algorithms may serve as bridges between current and future missions.

List of Acronyms and Abbreviations

DDA Discrete Dipole Approximation
DSD Drop Size Distribution
GMI GPM Microwave Imager
GPM Global Precipitation Measurement
HB Hitschfeld-Bordan
IMPACTS The Investigation of Microphysics and Precipitation for Atlantic Coast-Threatening Snowstorms
IWC Ice Water Content
ML Machine Learning
MS Multiple Scattering
NetCDF Network Common Data Form
NUBF Non-Uniform Beam Filling **NASA** National Aeronautics and Space Administration
PIA Path Integrated Attenuation
PSD Particle Size Distribution
PWC Precipitation Water Content

SRT Surface Reference Technique
TRMM Tropical Rainfall Measuring Mission

References

[1]   Weinman JA, Meneghini R, Nakamura K. Retrieval of precipitation profiles from airborne radar and passive radiometer measurements: Comparison with dual-frequency radar measurements. Journal of Applied Meteorology. 1990; 200(29): 981 – 993.
[2]   Hitschfeld W, Bordan J. Errors inherent in the radar measurement of rainfall at attenuating wavelengths. Journal of Atmospheric Sciences. 1954; 11(1): 58–67.
[3]   Meneghini R, Eckerman J, Atlas D. Dermination of Rain Rate from a Space-borne Radar Using Measurements of Total Attenuation. IEEE Transactions on Geoscience and Remote Sensing.1983;GE-21: 34–43.
[4]   Fujita M, Okamoto K, Yoshikado S, Nakamura K. Inference of rain rate profile and path-integrated rain rate by an airborne microwave rain scatterometer. Radio Science. 1985; 20(3): 631–642.
[5]   Smith E, Turk FJ, Farrar M, Mugnai A, Xiang X. Estimating 13.8-GHz pathintegrated attenuation from 10.7-GHz brightness temperatures for the TRMM combined PRTMI precipitation algorithm. Journal of Applied Meteorology. 1997; 36: 365–388.
[6]   Kummerow CK. The Tropical Rainfall Measuring Mission (TRMM) sensor package. Journal of Atmospheric and Oceanic Technology. 1998; 15: 809–817.
[7]   Haddad Z. The TRMM day-1 radar/radiometer combined rain-profiling algorithm. Journal of the Meteorological Society of Japan. 1997; 75: 799–809.
[8]   Grecu M, Olson WS, Anagnostou E. Retrieval of precipitation profiles from multiresolution, multifrequency active and passive microwave observations. Journal of Applied Meteorology. 2004; 43: 562–575.
[9]   Masunaga H. Combined radar and radiometer analysis of precipitation profiles for a parametric retrieval algorithm. Journal of Atmospheric and Oceanic Technology. 2005; 22: 909–929.
[10]   Munchak J. A modular optimal estimation method for combined radar-radiometer precipitation profiling. Journal of Applied Meteorology and Climatology. 2001; 50: 433–448.
[11]   Grecu M, Olson W.S. Bayesian estimation of precipitation from satellite passive microwave observations using combined radar retrievals. Journal of Applied Meteorology and Climatology. 2006; 45: 416–433.
[12]   Kummerow C. An observationally generated a priori database for microwave rainfall retrievals. Journal of Atmospheric and Oceanic Technology. 2011; 28: 113–130.
[13]   Hou A. The global precipitation measurement mission. Bulletin of the American Meteorological Society. 2014; 95: 701–722.
[14]   Marshall JS, Palmer WMK. The distribution of raindrops with size. J. Meteorol. 1948; 5: 165–166.

[15]   Ulbrich CW. Natural variations in the analytical form of the raindrop size distribution. Journal of climate and applied meteorology. 1983; 22(10): 1764–1775.

[16]   Sekhon RS, Srivastava RC. Snow Size Spectra and Radar Reflectivity. Journal of Atmospheric Sciences. 1970; 27(2): 299–307.

[17]   Heymsfield A. Precipitation Development in Stratiform Ice Clouds: A Microphysical and Dynamical Study Journal of Atmospheric Sciences. 1977; 34(2): 367–381.

[18]   Meneghini R, Kozu T. Spaceborne weather radar. Boston: Artech House Publ. 1990; ISBN: 0890063826.

[19]   Bohren CF, Huffman DR. Absorption and scattering of light by small particles. John Wiley and Sons. 2008.

[20]   Mishchenko MI, Travis LD, Lacis AA. Scattering, absorption, and emission of light by small particles. Cambridge university press. 2002.

[21]   Battan LJ. Radar observation of the atmosphere. 1973.

[22]   Tyynelä J, Leinonen J, Moisseev D, Nousiainen T. Radar backscattering from snowflakes: Comparison of fractal, aggregate, and soft spheroid models. Journal of Atmospheric and Oceanic Technology. 2011 Nov;28(11):1365-72.

[23]   Liu G. Approximation of single scattering properties of ice and snow particles for high microwave frequencies. Journal of the atmospheric sciences. 2004;61(20):2441-56.

[24]   Kuo KS, Olson WS, Johnson BT, Grecu M, Tian L, Clune TL, van Aartsen BH, Heymsfield AJ, Liao L, Meneghini R. The Microwave Radiative Properties of Falling Snow Derived from Nonspherical Ice Particle Models. Part I: An Extensive Database of Simulated Pristine Crystals and Aggregate Particles, and Their Scattering Properties Journal of Applied Meteorology and Climatology. 2016;55(3):691-708.

[25]   Draine BT, Flatau PJ. Discrete-dipole approximation for scattering calculations. Josa A. 1994;11(4):1491-9.

[26]   Trefethen LN. Spectral methods in MATLAB. Society for industrial and applied mathematics; 2000.

[27]   Hogan RJ, Honeyager R, Tyynelä J, Kneifel S. Calculating the millimetre-wave scattering phase function of snowflakes using the self-similar Rayleigh–Gans Approximation. Quarterly Journal of the Royal Meteorological Society. 2017;143(703):834-44.

[28]   Rosenkranz PW. Water vapor microwave continuum absorption: A comparison of measurements and models. Radio Sci. 1998; 33: 919–928.

[29]   Testud J, Oury, S, Black RA, Amayenc P, Dou X. The Concept of "Normalized" Distribution to Describe Raindrop Spectra: A Tool for Cloud Physics and Cloud Remote Sensing. Journal of Applied Meteorology. 2001; 40(6): 1118–1140.

[30]   Bringi VN, Chandrasekar V, Hubbert J, Gorgucci E, Randeu WL, Schoenhuber M. Raindrop size distribution in different climatic regimes from disdrometer and dual-polarized radar analysis. Journal of the atmospheric sciences. 2003;60(2):354-65.

[31]   Ferreira F, Amayenc P, Oury S, Testud J. Study and tests of improved rain estimates from the TRMM precipitation radar. Journal of Applied Meteorology. 2001;40(11):1878-99.

[32]   Raupach, Berne A. Invariance of the Double-Moment Normalized Raindrop Size Distribution through 3D Spatial Displacement in Stratiform Rain. J. Appl. Meteor. Climatol. 2017; 56; 1663–1680.

[33]   McMurdie LA, Heymsfield GM, Yorks JE, Braun SA, Skofronick-Jackson G, Rauber RM, Yuter S, Colle B, McFarquhar GM, Poellot M, Novak DR. Chasing Snowstorms: The Investigation of Microphysics and Precipitation for Atlantic Coast-Threatening Snowstorms (IMPACTS) Campaign. Bulletin of the American Meteorological Society. 2022;103(5):248-74.

[34]   Iguchi T, Meneghini R. Intercomparison of single-frequency methods for retrieving a vertical rain profile from airborne or spaceborne radar data. Journal of Atmospheric and Oceanic Technology. 1994;11(6):1507-16.

[35]   Meneghini R, Eckerman J, Atlas D. Determination of Rain Rate from a Spaceborne Radar Using Measurements of Total Attenuation. IEEE Transactions on Geoscience and Remote Sensing. 1983; 21: 34-43.

[36]   Marzoug M, Amayenc P. Improved range-profiling algorithm of rainfall rate from a spaceborne radar with path-integrated attenuation constraint. IEEE Transactions on Geoscience and Remote Sensing. 1981; 29(4): 584-592.

[37]   Iguchi T, Seto S, Meneghini R, Yoshida N, Awaka J, Le M, Chandrasekar V, Kubota T. GPM/DPR Level-2 Algorithm Theoretical Basis Document; NASA Technical Report. 2018. Available online: https://gpm.nasa.gov/resources/documents/gpmdpr-level-2-algorithm-theoretical-basis-document-atbd

[38]   Iguchi T, Kozu T, Meneghini R, Awaka J, Okamoto KI. Rain-profiling algorithm for the TRMM precipitation radar. Journal of applied meteorology. 2000;39(12):2038-52.

[39]   Tarantola A. Inverse problem theory and methods for model parameter estimation. Society for industrial and applied mathematics. 2005.

[40]   Grecu M, Anagnostou EN. Use of Passive Microwave Observations in a Radar Rainfall-Profiling Algorithm. Journal of Applied Meteorology. 2002: 41(7): 702-715.

[41]   Marzano FS, Mugnai A, Panegrossi G, Pierdicca N, Smith EA, Turk J. Bayesian estimation of precipitating cloud parameters from combined measurements of spaceborne microwave radiometer and radar. IEEE Transactions on Geoscience and Remote Sensing. 1999;37(1):596-613.

[42]   Kummerow C. On the accuracy of the Eddington approximation for radiative transfer in the microwave frequencies. Journal of Geophysical Research: Atmospheres. 1993;98(D2):2757-65.

[43]   Liu Q, Simmer C, Ruprecht E. Three-dimensional radiative transfer effects of clouds in the microwave spectral range. Journal of Geophysical Research: Atmospheres. 1996;101(D2):4289-98.

[44]   Grecu M, Olson WS, Munchak SJ, Ringerud S, Liao L, Haddad Z, Kelley BL, McLaughlin SF. The GPM combined algorithm. Journal of Atmospheric and Oceanic Technology. 2016;33(10):2225-45.

[45]   Gelb, A. Applied Optimal Estimation. The M.I.T. Press. 1974.

[46]   Bertsekas D. Nonlinear Programming. Athena Scientific; 2016.

[47]   Evensen G. Data assimilation: the ensemble Kalman filter. Berlin: springer; 2009.

[48]   Doicu A, Trautmann T, Schreier F. Numerical regularization for atmospheric inverse problems Springer Science and Business Media. 2010.

[49]   Maahn M, Turner, DD, Löhnert U, Posselt DJ, Ebell K, Mace GG, Comstock JM. Optimal Estimation Retrievals and Their Uncertainties: What Every Atmospheric Scientist Should Know. Bulletin of the American Meteorological Society. 2020; 101(9): E1512-E1523.

[50]   Iguchi T, Kozu T, Kwiatkowski J, Meneghini R, Awaka J, Okamoto KI. Uncertainties in the rain profiling algorithm for the TRMM precipitation radar. Journal of the Meteorological Society of Japan. Ser. II. 2009;87:1-30.

[51]   Hogan RJ, Battaglia A. Fast lidar and radar multiple-scattering models: Part 2: Wide-angle scattering using the time-dependent two-stream approximation. J. Atmos. Sci. 2008; 65: 3636-3651

[52]   Yang W, Zhang X, Tian Y, Wang W, Xue JH, Liao Q. Deep learning for single image super-resolution: A brief review. IEEE Transactions on Multimedia. 2019;21(12):3106-21.

[53]   Skofronick-Jackson G, Petersen WA, Berg W, Kidd C, Stocker EF, Kirschbaum DB, Kakar R, Braun SA, Huffman GJ, Iguchi T, Kirstetter PE. The Global Precipitation Measurement (GPM) mission for science and society. Bulletin of the American Meteorological Society. 2017;98(8):1679-95.

[54]   Draper DW, Newell DA, Wentz FJ, Krimchansky S, Skofronick-Jackson GM. The global precipitation measurement (GPM) microwave imager (GMI): Instrument overview and early on-orbit performance. IEEE Journal of Selected Topics in Applied Earth Observations and Remote Sensing. 2015;8(7):3452-62.

[55]   Meneghini R, Kim H, Liao L, Jones JA, Kwiatkowski JM. An initial assessment of the surface reference technique applied to data from the dual-frequency precipitation radar (DPR) on the GPM satellite. Journal of Atmospheric and Oceanic Technology. 2015; 32(12): 2281-2296.

[56]   Meneghini R, Iguchi T, Kozu T, Liao L, Okamoto KI, Jones JA, Kwiatkowski J. Use of the surface reference technique for path attenuation estimates from the TRMM precipitation radar. Journal of Applied Meteorology. 2000;39(12):2053-70.

[57]   Géron A. Hands-on machine learning with Scikit-Learn, Keras, and TensorFlow. O'Reilly Media, Inc. 2022.

[58]   Seto S, Iguchi T, Meneghini R, Awaka J, Kubota T, Masaki T, Takahashi N. The precipitation rate retrieval algorithms for the GPM Dual-frequency Precipitation Radar. Journal of the Meteorological Society of Japan. Ser. II. 2021.

[59]   Goodfellow I, Bengio Y, Courville A. Deep learning. MIT press. 2016.

[60]   Abdai M, et al. TensorFlow: Large-scale machine learning on heterogeneous systems, Software available from tensorflow.org. 2015

[61]   Peral E, Tanelli S, Statham S, Joshi S, Imken T, Price D, Sauder J, Chahat N, Williams A. RainCube: the first ever radar measurements from a CubeSat in space. Journal of Applied Remote Sensing. 2019 Jun;13(3):032504.

[62]   Blackwell WJ, Braun S, Bennartz R, Velden C, DeMaria M, Atlas R, Dunion J, Marks F, Rogers R, Annane B, Leslie RV. An overview of the TROPICS NASA earth venture mission. Quarterly Journal of the Royal Meteorological Society. 2018 Nov;144:16-26.

[63]   Gong J, Wu DL, Eriksson P. The first global 883 GHz cloud ice survey: IceCube Level 1 data calibration, processing and analysis. Earth System Science Data. 2021 Nov 18;13(11):5369-87.